

The H₂ Glow of a Quiescent Molecular Cloud Observed with JWSTPAUL F. GOLDSMITH,¹ SHENGZHE WANG,^{2,3} XIN WANG,^{2,3,4} RAPHAEL SKALIDIS,^{1,5,*} GARY A. FULLER,^{6,7} DI LI,^{8,9,10,11}
CHAO-WEI TSAI,^{3,4,2} LILE WANG,^{12,13} AND DONGHUI QUAN¹⁴¹*Jet Propulsion Laboratory, California Institute of Technology, 4800 Oak Grove Drive, Pasadena, CA 91109, USA*²*School of Astronomy and Space Science, University of Chinese Academy of Sciences (UCAS), Beijing 100049, China*³*National Astronomical Observatories, Chinese Academy of Sciences, Beijing 100101, China*⁴*Institute for Frontiers in Astronomy and Astrophysics, Beijing Normal University, Beijing 102206, China*⁵*TAPIR, Mailcode 350-17, California Institute of Technology, Pasadena, CA 91125, USA*⁶*Jodrell Bank Centre for Astrophysics, Department of Physics and Astronomy, The University of Manchester, Oxford Road, Manchester M13 9PL, UK*⁷*I. Physikalisches Institut, University of Cologne, Zùlpicher Str. 77, 50937 Köln, Germany*⁸*Department of Astronomy, Tsinghua University, Beijing 100084, People's Republic of China*⁹*National Astronomical Observatories, Chinese Academy of Sciences, Beijing 100101, People's Republic of China*¹⁰*Research Center for Astronomical Computing, Zhejiang Laboratory, Hangzhou 311100, People's Republic of China*¹¹*New Cornerstone Science Laboratory, Shenzhen 518054, People's Republic of China*¹²*The Kavli Institute for Astronomy and Astrophysics, Peking University, Beijing 100871, People's Republic of China*¹³*Department of Astronomy, School of Physics, Peking University, Beijing 10087, People's Republic of China*¹⁴*Zhejiang Laboratory, Hangzhou 311121, People's Republic of China*

ABSTRACT

We report JWST MIRI/MRS observations of the H₂ $S(1)$ 17.04 μm transition in two regions in the boundary of the Taurus Molecular Cloud. The two regions, denoted “Edge” (near the relatively sharp boundary of the ^{13}CO $J = 1 \rightarrow 0$ emission) and “Peak” (the location of the strongest H₂ emission observed with *Spitzer*), have average intensities of 14.5 MJy sr^{−1} and 32.1 MJy sr^{−1}, respectively. We find small scale structures of characteristic size 1.0″–2.5″, corresponding to 140 AU–350 AU, with characteristic intensity above the extended background of 10 MJy sr^{−1}, corresponding to a $J = 3$ column density of $1.6 \times 10^{17} \text{ cm}^{-2}$. The most plausible explanation for the observed intensities from level 845 K above the $J = 1$ ortho–H₂ ground state level is excitation by collisions with H₂ molecules (the hydrogen in this region being predominantly molecular). Two mechanisms, turbulent dissipation and shocks, have been proposed for heating of localized regions of the ISM to temperatures $\simeq 1000$ K to explain abundances of and emission from particular molecules. While we cannot determine unique values of density and kinetic temperature, the solutions in best agreement with predictions of shock models are $n(\text{H}_2) = 370 \text{ cm}^{-3}$ and $T_{\text{kin}} = 1000 \text{ K}$. The total H₂ column density of the small-scale structures under these conditions is $\simeq 8 \times 10^{17} \text{ cm}^{-2}$. This first direct detection of tiny scale structure in the quiescent molecular interstellar medium has significant implications for the physical structure of this phase of the ISM and the maintaining of supersonic motions within it.

Keywords: Interstellar medium (847); shocks; Interstellar line emission (844); Molecular clouds (1072)

1. INTRODUCTION

Understanding the small-scale structure of the interstellar medium (ISM) is fundamental for many reasons. On scales smaller than 100 AU, different physical processes may reveal themselves, including the dissipation of turbulence (Falgarone et al. 2007; Godard et al. 2009, 2014) and the fragmentation of gas (Beuther et al. 2019, and references therein) during the process of star formation. Very small-scale structure has been seen in atomic and ionized phases

Corresponding author: Paul Goldsmith, Xin Wang

paul.f.goldsmith@jpl.nasa.gov, xwang@ucas.ac.cn

* Hubble Fellow

of the ISM, as discussed in the reviews by Heiles & Stinebring (2007) and Stanimirović & Zweibel (2018). For atomic gas, these are referred to as Tiny Scale Atomic Structure (TSAS) and for ionized gas, Tiny Scale Ionized Structure.

Radio pulsars are a convenient background source for observations of optical depth variations of 21cm absorption, and combined with multi-epoch observations and their proper motion allow probing variations on quite small angular scales (Frail et al. 1994) but see Stanimirovic et al. (2004); Stanimirović et al. (2010). Variations have recently been observed down to scales ≤ 20 pc (Liu et al. 2021). VLBI observations of extended background radio sources allow direct imaging of variations in the 21 cm signal, which are felt likely to be due to opacity variations on a scale of 25 AU Brogan et al. (2007). Fluctuations in the column density of ionized gas can produce lensing that changes the observed flux of distant radio sources and changes in pulsar dispersion measure characterized as Extreme Scattering Events (ESE) suggest structure on a scale of 10's to 100's of AU (Stanimirović & Zweibel 2018).

Much more limited studies of the Tiny Scale Molecular Structure (TSMS) have been carried out. Marscher et al. (1993) and Moore & Marscher (1995) have reported time variations in the 6 cm H_2CO absorption profile against two radio sources that indicate structure in the molecular ISM on the order of 10 AU in size. Optical and UV absorption lines (Savage et al. 1977; Wakker 2006; Stanimirović & Zweibel 2018) probe extremely fine lines of sight, and while they do not as readily lend themselves to studying variations and structures in the absorbing gas, people have looked for variability in absorbing features (e.g. Farhang et al. 2023).

The nature of the material producing the observed very small-scale variations in the diffuse ISM remains controversial. It is possible rather than being discrete structures of a characteristic size these are the tail of a distribution of turbulent variations (Deshpande 2007). The relationship of very small-scale structure in the atomic and ionized ISM to that in the denser, cooler molecular ISM remains unclear, with imaging of the latter being so limited. This situation has begun to change in the past few years.

Molecular hydrogen is the dominant constituent of the molecular ISM. Ground-based facilities have allowed observations with subarcsecond angular resolution of H_2 rotational and rovibrational emission from shocks (Santangelo et al. 2014), jets (Lorenzetti et al. 2003), and small-scale clumps (Vannier et al. 2001; Lacombe et al. 2004) in the central region of Orion OMC1. Velocity-resolved H_2 has been observed towards shocked regions (Neufeld et al. 2024). Gry et al. (2002) and Falgarone et al. (2005) have observed H_2 emission along relatively long paths through the Galactic ISM, suggesting that this may be relatively common in the Milky Way.

Goldsmith et al. (2010) observed the nearby ($D \simeq 140$ pc¹) Taurus Molecular Cloud; using *Spitzer* IRS with a large extraction aperture several transitions were detected, but the low angular resolution precluded being able to draw any conclusions about the size of the structures producing the hot H_2 observed. The Taurus molecular cloud can reasonably be characterized as quiescent, in that among the ~ 400 stars accepted as being in the region defined by CO emission and dust extinction, there are 6 G type stars and 2 B type stars, with the remaining stars being later-type (Güdel et al. 2007). This means that there is little stellar UV produced (Xia et al. 2022), and gas temperatures throughout the cloud are low, ≤ 15 K (Goldsmith et al. 2010) as are dust temperatures (12 K – 15 K; Flagey et al. (2009)).

Molecular outflows, associated with early phases of protostars, are rare in Taurus, with only 20 known (Narayanan et al. 2012). These may be capable of sustaining the observed supersonic (turbulent) linewidths in Taurus (Section 5.2 and Appendix A), but do not produce multi-km s⁻¹ perturbations of the velocity field of the cloud. There does not appear to be evidence of cloud-scale expansion or contraction although there is possible rotation, based on the kinematics of stars associated with the Taurus molecular cloud (Galli et al. 2019).

Observations of very small-scale structure analogous to those seen in the atomic ISM but in the cooler and denser molecular ISM, and which are predicated theoretically to be sites of turbulent dissipation (e.g. Godard et al. 2009), are critical for understanding the energetics of these regions in which star formation occurs, but have to date been elusive. The situation has now changed dramatically with the availability of the MIRI MRS instrument (Wright et al. 2023) on the JWST (Gardner et al. 2023). For example, pure rotational transitions of H_2 from $S(1)$ through $S(8)$ have been observed in a protoplanetary disk by Berné et al. (2023). At the 17.035 μm wavelength of the $S(1)$ pure rotational line of H_2 , JWST/MIRI offers 0.7'' angular resolution, corresponding to a spatial resolution of $\simeq 100$ AU or 1.5×10^{15} cm at the 140 pc distance of the Taurus Molecular Cloud, along with a spectral resolving power R equal to 2500. We have used these capabilities of JWST to study the H_2 $S(1)$ emission from two regions in the boundary of

¹ The Taurus cloud has a significant line of sight extent, estimated for the main region of the cloud to be 130 pc to 172 pc by Galli et al. (2019) and 131 to 168 pc by Zucker et al. (2021). The largest values are for relatively limited, isolated regions. The distance of Heiles Cloud 2, relatively close to the positions we have observed is between 138 and 142 pc (Galli et al. 2019). We adopt the 140 pc value as likely appropriate for the boundary region we have observed and for consistency with previous studies.

the Taurus Molecular Cloud that had previously been observed with much lower angular and spectral resolution using *Spitzer* (Goldsmith et al. 2010).

Our goal is to study the properties of H₂ emission at scales where energy dissipation occurs. Such regions representative of the general ISM were previously inaccessible for this type of investigation, but now, thanks to the high angular resolution and sensitivity of JWST, are possible. We observed only a single transition, but have resolved the small-scale (dissipation) fluctuations of the H₂ emission. While nominally lying in the quiescent boundary of the molecular cloud, the fact that the H₂ $J = 3$ level lies $\simeq 845$ K above the ortho-H₂ ground state level demands significantly different excitation than that characterizing the 10 K – 50 K CO (Goldsmith et al. 2008) seen in the same direction.

This paper is organized as follows. In §2 we discuss the JWST data taking and processing, although details are given in the Appendix. In §3 we discuss the procedure we have used to derive the column density of H₂ emission. In §4 we present a brief analysis of different mechanisms that may be responsible for excitation of the $S(1)$ line and the implications for the total column density of excited H₂ molecules. In §5 we discuss possible sources for the high temperatures that are required for collisional excitation of H₂. In §6 we summarize and discuss our results. In the Appendices we give details on the MIRI/MRS data processing and on the ¹²CO and ¹³CO emission seen in the same direction as the observed H₂.

2. JWST DATA

The data discussed here were acquired by the JWST Cycle-2 Program GO-3050 (PI Goldsmith). Two regions at the straight edge boundary seen in ¹³CO were observed; these had been previously observed by Goldsmith et al. (2010) using *Spitzer*. Figure 1 shows the two regions observed overlaid on an image of the ¹³CO $J = 1 \rightarrow 0$ integrated intensity. The “Edge” position is approximately at the position of marked drop in the integrated intensity of ¹³CO emission. The “Peak” position includes a region at the distance from the cloud edge at which the strongest $S(0)$ emission was found with *Spitzer*. Table 1 gives the coordinates of the regions observed.

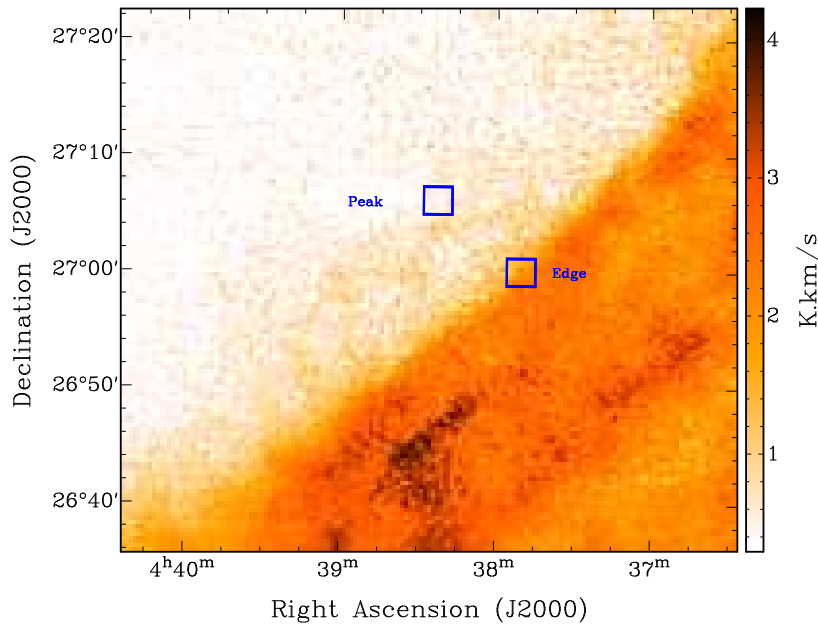


Figure 1. The two regions observed in the H₂ $S(1)$ transition in the boundary of the Taurus Molecular Cloud overlaid on an image of the ¹³CO $J = 1 \rightarrow 0$ integrated intensity (adapted from Goldsmith et al. 2008). The size of the regions, denoted “Edge” and “Peak” has been significantly expanded to make them visible.

The MIRI Medium Resolution Spectrometer (MRS) consists of four channels that span the range 4.9 to 27.9 μm . The wavelength range of MRS covers four emission lines detectable in the *Spitzer* observations: the $S(0)$ line at 28.22 μm

Table 1. Sources Observed in the Taurus Boundary Region

Source	$\alpha(2000)$			$\delta(2000)$		
	(h	m	s)	($^{\circ}$	'	")
Peak	04	37	50.40	+27	00	02.5
Edge	04	38	22.75	+27	06	12.0

(sub-band C, Channel 4), the $S(1)$ line at $17.04 \mu\text{m}$ (sub-band C, Channel 3), the $S(2)$ line at $12.2 \mu\text{m}$ (sub-band A, Channel 3), and the $S(3)$ line at $9.67 \mu\text{m}$ (sub-band B, Channel 2). Considering that the $S(0)$ line is at the far red edge of Channel 4 sub-band C, and the $S(3)$ line is much weaker (a factor of a few hundred weaker than $S(1)$), our focus was primarily on the detection of the $S(1)$ and $S(2)$ lines. These lines are distributed across Channel 3 sub-band C (with a wavelength range of $15.41 - 17.98 \mu\text{m}$) and Channel 3 sub-band A (with a wavelength range of $11.55 - 13.47 \mu\text{m}$).

The FoV of MRS Channel 3 is $5.2'' \times 6.2''$, whereas the previous *Spitzer* IRS extraction aperture covers $10.7'' \times 108''$. To mitigate the giant leap in angular resolution from the *Spitzer* IRS observations to the MRS imaging spectroscopy, we designed a mosaic consisting of 4 by 4 individual MRS footprints for each sub-band C visit. As a result, our FoV is expanded to $17.7'' \times 20.4''$ for the primary MRS observations in each region. We utilized a single MRS pointing (with FoV $5.2'' \times 6.2''$) to perform deep sub-band A exposures necessary to detect the much weaker $S(2)$ line.

Observations were conducted for both the Peak and Edge regions, targeting the $S(1)$ and $S(2)$ transitions. For $S(1)$, the mosaicing was combined with a 4-point dither pattern. Each exposure lasted 510 seconds, leading to a total exposure time of 8160 seconds. Additionally, background observations were performed for $S(1)$ with an identical exposure time and using the same 4-point dither pattern. The background observation region was selected based on prior *Spitzer* results.

For $S(2)$, observations were split into two separate exposures, each using the 4-point dither pattern with an exposure duration of 7549 seconds, resulting in a total exposure time of 15,098 seconds. During the observations, an anomaly occurred in the $S(2)$ observation of the Peak region. Consequently, we only obtained $S(2)$ results for the Edge region, and these will be discussed in a separate paper.

A 10% overlap between adjacent pointings was recommended by the STScI program scientist to ensure contiguous coverage for mosaicing. As discussed in Appendix A, the actual overlap for the Band 3 spectra that included the $17.07 \mu\text{m}$ $S(1)$ line was much greater, in excess of 60 %. This resulted in a slightly non-uniform sensitivity across the mosaiced area. This worked very well, with minimal obvious artifacts within all but the edges of the mosaic. In the portions of the mosaic within 3 pixels of the edge there was a sufficient number of pixels with obviously erroneously high values that we ended up removing edge strips from the final image. This may be due in part to the smaller integration time at the edges of the mosaic, as discussed in Appendix A.

The spectral baselines were excellent due to the subtraction of nearby reference position. This is seen in Figure 2, which covers essentially the entire JWST/MIRI Channel 3–Long output. The region around the $S(1)$ line is not confused by any other spectral lines, and the H_2 line is readily apparent. The baseline on both sides of the $S(1)$ line was very flat so that only a linear spectral baseline was required to completely remove any continuum signal. This was done by fitting a 1^{st} order polynomial to 5 channels on each side of the $S(1)$ line starting 5 channels from the channel closest to the rest wavelength of the line. An expanded view of the region around the $S(1)$ line is shown in Figure 3, again illustrating the very high quality of the spectral baseline. To obtain the total intensity in the $S(1)$ line, we summed the data from five channels centered on that closest to the wavelength of the $S(1)$ line. Additional information on data processing is given in Appendix A. The resulting images are shown in Figures 4 and 5.

The sensitivity of the JWST/MIRI instrument and the exposure time of over 4 hours per region resulted in very significant detection of the $S(1)$ line throughout most of the FOV covering both Edge and Peak regions, although the latter is significantly stronger.

Figure 6 shows the distribution of intensities for the sum of the five channels “on” the line (line; blue) and 10 channels “off” the line (background; green). The statistics of the observations are summarized in Table 2.

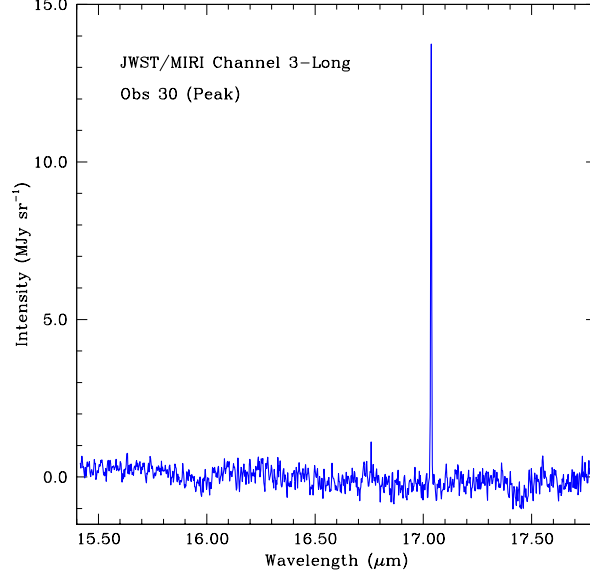


Figure 2. Output covering essentially entire spectral range of JWST/MIRI Channel 3-Long from the Peak Region of the Taurus Molecular Cloud integrated over the area of the mosaiced observation. Only a linear baseline has been removed. The H₂ S(1) emission is the only strong line that is visible.

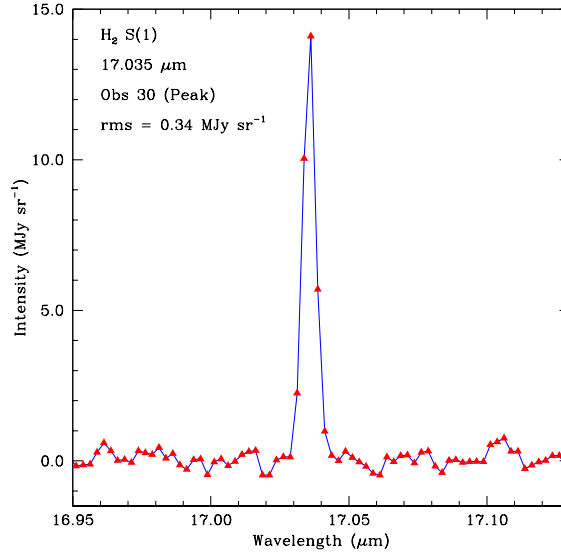


Figure 3. Expanded view of emission around the wavelength of the H₂ 17 μ m S(1) line from the Peak Region of the Taurus Molecular Cloud integrated over the area of the mosaiced observation. Only a linear baseline has been removed. Note that for a resolving power R equivalent to a velocity resolution of 120 km s⁻¹ the observed spectrum is essentially the response of the MIRI spectrometer rather than being the emission line profile.

We see a very small (<1 MJy sr⁻¹) residual background that remained after subtracting data from reference region from the two mosaics of the Taurus boundary region. This was essentially a constant function of wavelength and was removed by fitting a linear baseline to the spectrum of each pixel of the mosaics. Pixels with line intensities greater than $\simeq 5$ MJy sr⁻¹ are statistically significant detections, which includes most of the positions in the Edge region and almost all of the positions in the Peak region. As indicated by the extreme values of maximum and minimum intensity,

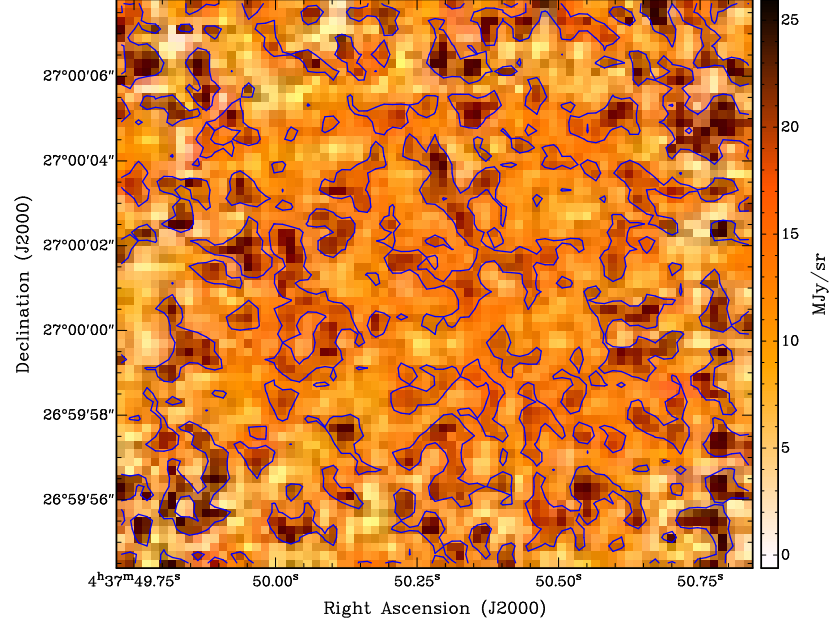


Figure 4. H_2 $S(1)$ emission from Edge Region of the Taurus Molecular Cloud. The contours are at a level of 20 MJy sr^{-1}

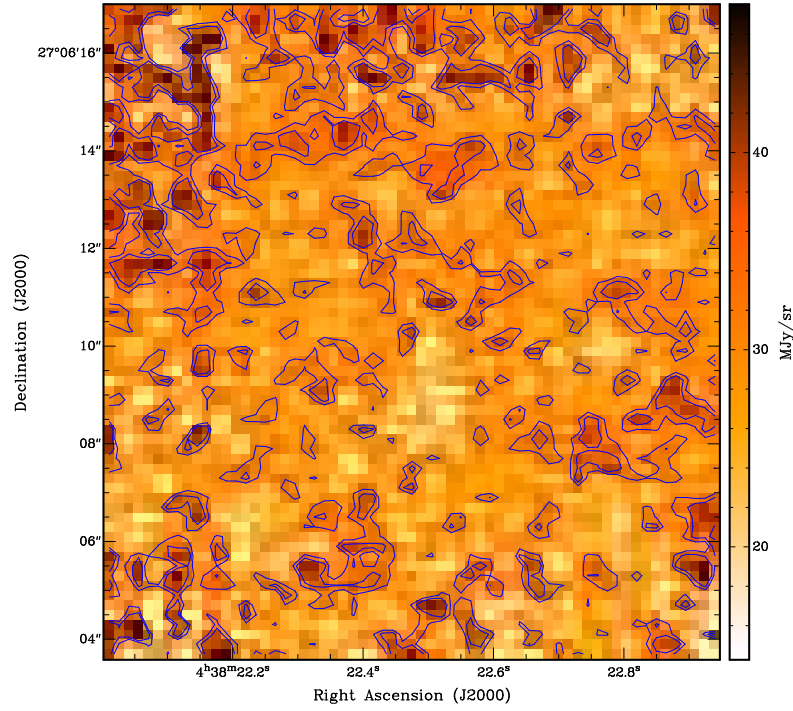


Figure 5. H_2 $S(1)$ emission from Peak Region of the Taurus Molecular Cloud. The contours are at levels of 30 and 36 MJy sr^{-1} .

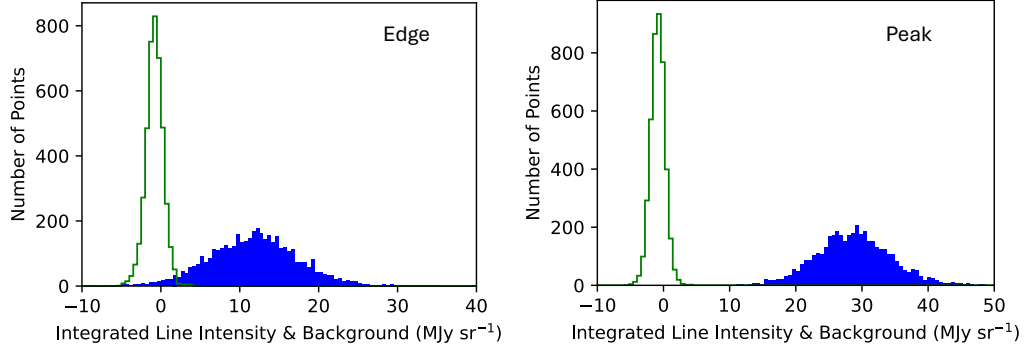


Figure 6. Distribution of intensity from off-line (“background”) channels (green) and summed on-line (“line”) channels (blue) for the Edge (left) and Peak (right) regions in the Taurus Molecular Cloud boundary.

Table 2. Statistics of Observations of the $S(1)$ H₂ line in the Taurus Boundary

Parameter ^a	Edge Region	Peak Region
$\langle \text{background} \rangle$	-0.8	-0.9
$\sigma(\text{background})$	1.1	1.1
$\min(\text{background})$	-5.4	-5.7
$\max(\text{background})$	4.0	4.1
$\langle \text{line} \rangle^b$	12.6	29.6
$\sigma(\text{line})$	5.6	5.8
$\min(\text{line})$	-18.2	4.8
$\max(\text{line})$	35.7	54.9
$\langle \text{line} \rangle / \langle \text{background} \rangle$	11.5	26.9

^a Intensities in MJy sr⁻¹

^b Sum over 5 channels as illustrated by Figure 3

there are still some defective pixels. But from the distributions shown in Figure 6, it is clear that these are a very small fraction of the pixels in the images of the two regions.

The mean intensities correspond to column densities $N(J = 3) = 2.3 \times 10^{17} \text{ cm}^{-2}$ in the Edge region and $5.1 \times 10^{17} \text{ cm}^{-2}$ in the Peak region. For comparison, the column density derived from *Spitzer* data in the Edge region was $1.0 \times 10^{17} \text{ cm}^{-2}$, and in the Peak region was $1.6 \times 10^{17} \text{ cm}^{-2}$ (Goldsmith et al. 2008). Thus, the present results

are a factor 2–3 times greater. The much larger extraction aperture used for *Spitzer* data reduction compared to size of JWST images as well as instrument calibrations are plausible contributors to this difference.

Beyond confirming the presence of highly excited H₂ in the Taurus boundary initially detected by *Spitzer*, the outstanding feature of the emission imaged by JWST in Figures 4 and 5 is the presence of small scale structures. These show a variety of shapes, with sizes in the range between 1.0'' and 2.5'', corresponding to physical dimensions 140 to 350 AU. We discuss some of the characteristics of these clumps determined by the H₂ emission below. The sizes are consistent with results of analysis using power spectrum and other techniques; these are discussed in more detail in a paper currently in preparation. We feel the convincing detections in two regions do suggest that such small scale structures may be common throughout the molecular interstellar medium.

3. COLUMN DENSITY OF H₂

3.1. $J = 3$ Column Density

We assume that the H₂ rotational line emission is optically thin². In this limit the column density in the upper level of the observed transition, N_u (cm⁻²), is related to the observed intensity I (erg s⁻¹cm⁻²sr⁻¹) by

$$N_u = \frac{4\pi I}{A_{u,l} h \nu} , \quad (1)$$

where $A_{u,l}$ is the spontaneous decay rate(s⁻¹), h is Planck's constant, and ν is the frequency of the transition (Hz). For the H₂ $J = 3 \rightarrow 1$ S(1) line, the lowest transition of ortho-H₂, $A_{3,1} = 4.76 \times 10^{-10}$ s⁻¹ and $\lambda = 17.035$ μ m (Roueff et al. 2019), corresponding to $\nu = 1.76 \times 10^{13}$ Hz. Although JWST/MIRI does not resolve the H₂ emission from interstellar clouds, the pipeline output is given in units of specific intensity, I_ν (erg s⁻¹cm⁻²sr⁻¹Hz⁻¹), with the relationship with the upper level column density thus being

$$N_u = \frac{4\pi I_\nu \delta \nu}{A_{u,l} h \nu} , \quad (2)$$

where $\delta \nu$ is the frequency resolution, taken to be the full width at half maximum of the spectral response curve. The ratio of the observed frequency ν to the frequency resolution $\delta \nu$ is the resolving power, R , so that the preceding equation can be written

$$N_u = \frac{4\pi}{A_{u,l} h R} I_\nu . \quad (3)$$

The resolving power of JWST/MIRI is wavelength dependent. We here adopt the value $R = 2500$, slightly above value 2443 of the fitted curve for spatially unresolved sources given by Jones et al. (2023), allowing for slight broadening due to the extended nature of the emission observed here.

The coefficient relating specific intensity to column density is 2.58×10^{34} cm⁻²/erg s⁻¹cm⁻²sr⁻¹Hz⁻¹ for the S(1) line with the above parameters. The specific intensity units of the JWST data output are MJy sr⁻¹. As 1 MJy sr⁻¹ = 1.0×10^{-17} erg s⁻¹cm⁻²sr⁻¹Hz⁻¹, the conversion we employ for the $J = 3$ upper level of the S(1) line is

$$N(J=3)(\text{cm}^{-2}) = N_u = 1.6 \times 10^{16} I_\nu(S(1)) \text{ (MJy sr}^{-1}) . \quad (4)$$

The intensity corresponding to a 1 MJy sr⁻¹ S(1) line observed with JWST/MIRI is 7.04×10^{-8} erg s⁻¹cm⁻²sr⁻¹.

4. H₂ EXCITATION AND TOTAL COLUMN DENSITY OF ORTHO-H₂

A number of different mechanisms have been proposed to populate the excited rotational levels of H₂ and explain the observed far-infrared line emission (e.g. Falgarone et al. 2005; Neufeld et al. 2006; Goldsmith et al. 2010). These include excitation by cosmic rays, absorption of UV radiation, radiative decay of newly-formed H₂, and collisional excitation. We here briefly discuss each of these. Figure 7 of Padovani et al. (2022) shows a schematic of several of the various mechanisms.

The total column density of ortho-H₂ relative to that in $J = 3$ level is determined by the excitation of the molecule. For H₂, only the lower rotational levels have significant population at even the highest temperatures considered. Since the spontaneous decay rates for vibration-rotation lines are 100 to 1000 times faster than those of the pure rotational

² For highly subthermal excitation and a line width of 1 km s⁻¹ a column density $N(\text{ortho-H}_2) \simeq 10^{25}$ cm⁻² is required to reach an optical depth of unity in the S(1) line, at least 5 orders of magnitude greater than we derive below.

transitions, the fractional populations of levels with $v \geq 1$ are negligible. For example, even in LTE at 1000 K, the population of the $v = 1, J = 1$ level with $\Delta E/k = 6149$ K is only 0.0025 of $v = 0, J = 1$, and drops precipitously at lower temperatures.

4.1. Cosmic Ray Excitation

Cosmic ray (CR) protons and electrons and the secondary electrons they produce can ionize H₂. Secondary electrons from CR protons and electrons can excite vibrational and electronic levels of H₂. These processes have been studied in some detail (e.g. Gredel & Dalgarno 1995), with Padovani et al. (2022) giving updates to rates and an overview discussion. The cosmic ray ionization rate, ζ_{cr} has been measured in a wide range of environments using different techniques. In dense clouds, Caselli et al. (2002) found that best-fit models had $5 \times 10^{-19} \leq \zeta_{cr} \leq 5.0 \times 10^{-18} \text{ s}^{-1}$, and Williams et al. (1998) determined $\zeta_{cr} = 5 \times 10^{-17} \text{ s}^{-1}$ in a sample of cores having densities $1\text{--}3 \times 10^4 \text{ cm}^{-3}$. Bialy et al. (2022) used ground-based observations of H₂ rovibrational transitions to derive an upper limit $\zeta_{cr} \leq 1.5\text{--}3.6 \times 10^{-16} \text{ s}^{-1}$ in the interiors of four clouds with column densities $N(\text{H}_2) = 10^{22} \text{ cm}^{-2}$. In less dense regions, the inferred cosmic ray ionization rate is considerably higher, ranging up to $4 \times 10^{-16} \text{ s}^{-1}$ (van der Tak et al. 2006), and even $\simeq 10^{-15} \text{ s}^{-1}$ (McCall et al. 2003; Oka et al. 2005).

A useful quantity for the analysis of H₂ excitation is the product of the spontaneous decay rate and the upper level volume density. Let us consider the ‘‘clumps’’ clearly seen in the image of the H₂ $S(1)$ intensity distribution. We take the line of sight path length of a clump to be equal to a typical transverse size of $1'' = 2.1 \times 10^{15} \text{ cm}$. With a characteristic value $I_\nu = 10 \text{ MJyr}^{-1}$, $N_u = 1.6 \times 10^{17} \text{ cm}$, and $n_u = 76 \text{ cm}^{-3}$. This yields for the product

$$n(3)A_{3,1} = 3.6 \times 10^{-8} \text{ cm}^{-3} \text{ s}^{-1} . \quad (5)$$

We carry out an approximate analysis by assuming that the excitation by secondary electrons from CR protons or electrons excites the H₂ molecule from its low- J state in the ground vibrational state to a vibrationally excited level with $v \geq 1$, but often higher. As mentioned above, the rovibrational transitions decay extremely rapidly compared to pure rotational transitions. Collisional deexcitation is less rapid than spontaneous decay given the densities in question, as discussed below. After being excited, there is thus a series of rovibrational decays. In this process, the ortho- and para-H₂ remain separate species. The ortho-H₂ could end up back in the $v = 1, J = 1$ state (having decayed from $v = 1, J = 1$ or $v = 1, J = 3$ state), but is more likely to have decayed to a higher- J state in $v = 0$, and to then cascade down via a series of pure rotational transitions.

Without doing a complex multilevel calculation we can obtain an upper limit to the rate of the population of the $v = 0, J = 3$ level by assuming that every excitation of H₂ results in an H₂ molecule in the $J = 3$ level. In this model, the rate equation for the $J = 3$ level in $v = 0$ is

$$n(1)\zeta_{cr}^e = n(3)A_{3,1} , \quad (6)$$

where ζ_{cr}^e is the cosmic ray excitation rate and we have assumed that all ortho-H₂ is essentially all in the $J = 1$ rotational level of the ground vibrational state due to the highly subthermal excitation. The ratio of the excitation rate to the cosmic rate ionization rate is $\simeq 2$ for H₂ column densities $\leq 10^{20} \text{ cm}^{-2}$, but drops by $\leq 10\%$ for H₂ column densities as large as 10^{22} cm^{-2} (Padovani et al. 2022)³.

We model a clump seen in the H₂ $S(1)$ emission with emission 5 MJy sr^{-1} above the extended emission, and in consequence a column density $N(3) = 8 \times 10^{16} \text{ cm}^{-2}$. Adopting a characteristic size of $1''$, we obtain the volume density $n(3) = 38 \text{ cm}^{-3}$, which yields $n(3)A_{3,1} \sim 1.8 \times 10^{-8} \text{ cm}^{-3} \text{ s}^{-1}$. Even if we assume the extreme conditions $\zeta_{cr} \simeq 1 \times 10^{-15} \text{ s}^{-1}$ and thus $\zeta_{cr}^e \simeq 2 \times 10^{-15} \text{ s}^{-1}$, with $\text{H}_2 \sim 1000 \text{ cm}^{-3}$, we obtain $n(1)\zeta_{cr}^e \ll n(3)A_{3,1}$. We conclude that cosmic ray excitation cannot be responsible for the observed H₂ emission.

4.2. UV Excitation

A general category of processes that can produce H₂ emission is the radiative cascade resulting from newly-formed H₂ molecules, with one source of such molecules being UV radiation. Modeling effect of UV on H₂ is complex, as the interaction of the radiation with the molecules can take many forms. In addition to external UV radiation, there is an internal radiation field produced by cosmic rays that can excite, photoionize, and photodissociate the H₂ (e.g.

³ The calculations of Padovani et al. (2022) are for H₂ in the $J = 0$ state as appropriate for very low OPR but the rates should not be very different for H₂ in $J = 1$.

Le Bourlot et al. 1995), although these processes can also be included as part of the effects of cosmic rays. Black & van Dishoeck (1987) considered the effects of UV in detail, but calculated only the emission in the near-infrared rovibrational transitions. The UV can excite the H_2 , which will result in a radiative cascade that populates the lower levels. If the H_2 is destroyed, it can reform, and in general a significant fraction of its binding energy goes to internal degrees of freedom, resulting in population of mid- to high-lying vibrational levels. These again cascade downwards and can produce emission in the pure rotational lines as well as the more often studied near-infrared rovibrational transitions. In some treatments of H_2 formation cascade, the process involved can be identified by the characteristic far-infrared emission spectrum (e.g. Tiné et al. 2003). In other models (Islam et al. 2010), the newly-formed H_2 is significantly vibrationally excited ($3 \leq v \leq 5$) but rotationally cool ($J = 1$ has by far the largest fractional population of ortho- H_2).

Takahashi & Uehara (2001) considered the effect of different types of grains on the distribution of formed H_2 over different internal states, and included pure rotational as well as rovibrational transitions. They modeled a cloud having total proton density of 10^3 cm^{-3} , but which was evolving from atomic to molecular form, and thus almost all hydrogen would be H^0 . For all models they considered, the intensity of the $S(1)$ line is $5.5\text{--}6.3 \times 10^{-8} \text{ erg s}^{-1} \text{ cm}^{-2} \text{ sr}^{-1}$. This is only about 1% of that corresponding to our detected intensity of 10 MJy sr^{-1} , indicating that even this situation with the maximum possible H_2 formation rate cannot explain the observed intensity.

A general treatment showing the inadequacy of formation cascade population of the $J = 3$ level can be shown using a similar treatment to that employed for analysis of cosmic ray excitation of H_2 . In this case, we assume that the H_2 formation rate is given by

$$\frac{dn(\text{H}_2)}{dt} = k_f n_{\text{H}} n(\text{H}^0) , \quad (7)$$

where k_f is the rate coefficient which is found to be $1.5\text{--}2.0 \times 10^{-17} \text{ cm}^3 \text{ s}^{-1}$ by Bialy et al. (2024), $n(\text{H}^0)$ is the atomic hydrogen density, and $n_{\text{H}} = n(\text{H}^0) + 2n(\text{H}_2)$. If we again assume that all newly-formed H_2 ends up in the $v = 1$, $J = 3$ level, the rate equation for the $J = 3$ level becomes

$$k_f n_{\text{H}} n(\text{H}^0) = n(3) A_{3,1} . \quad (8)$$

In the limit that essentially all hydrogen is atomic, we obtain the maximum rate into the $J = 3$ level, given by $k_f n^2(\text{H}^0) \text{ cm}^{-3} \text{ s}^{-1}$, and for $n(\text{H}^0) = 10^3 \text{ cm}^{-3}$, this rate is $2 \times 10^{-13} \text{ cm}^{-3} \text{ s}^{-1}$. This is 5 orders of magnitude less than the rate of transitions from $J = 3$ to $J = 1$, and confirms the inadequacy of formation cascade to explain the observations.

UV excitation (not involving H_2 destruction) can be more rapid due to trapping and effective reuse of photons, but the increase in the rate of populating the $J = 3$ level is still certainly less than required. If the H_2 were in chemical steady-state and destruction were dominated by UV, then the formation rate would be equal to the UV photodestruction rate. However, the UV radiation field in the boundary regions of Taurus is relatively low (Flagey et al. 2009), $0.3\text{--}2.8 \times$ the standard Habing radiation field ($1.6 \times 10^{-3} \text{ ergs}^{-1} \text{ cm}^{-2}$), and the resulting destruction rate would result in an even lower H_2 formation rate and cascade population of the $J = 1$ level than modeled above.

4.3. Collisional Excitation

Collisional excitation of H_2 rotational levels will certainly occur, with rate depending on temperature and density. The rate coefficients for collisions with H_2 calculated by Flower (1998) depend only very weakly on the spin modification of the colliding partner, which is assumed to be in $J = 0$ for para- H_2 and in $J = 1$ for ortho- H_2 . The gas-phase hydrogen in these regions of interest may not be entirely molecular, and in this case collisions with hydrogen atoms must be considered. The deexcitation rate coefficients calculated by Forrey et al. (1997) are approximately a factor of 3 smaller than those for collisional deexcitation by H_2 . The molecular hydrogen fraction in the regions observed is not known, and for simplicity we assume that the hydrogen is completely molecular. At a temperature of 300 K, assuming that the translational velocity distribution of the H_2 molecules is thermal, the critical density for the $S(1)$ line is 366 cm^{-3} , so that the excitation temperature of the transition is likely neither highly subthermal nor thermalized.

4.3.1. Ortho to Para Ratio

The total H_2 column density depends on the ortho-to-para (*OPR*) ratio of the H_2 , with the relationship between the total H_2 column density $N(\text{H}_2)$, the total column density of ortho- H_2 , $N(\text{ortho})$, and the *OPR* being

$$N(\text{H}_2) = N(\text{ortho})(1 + \text{OPR}^{-1}) . \quad (9)$$

In equilibrium at low temperatures, the *OPR* will be very small, while H₂ is formed with eV of energy, and thus is effectively hot, with *OPR* = 3, reflecting the ratio of statistical weights of the two spin modifications. Our data of a single transition cannot determine the *OPR* and observations of the *OPR* in quiescent H₂ are difficult and rare. Previous *Spitzer* observations of H₂ in this same region yielded *OPR* = 0.95 (Goldsmith et al. 2010).

The time-dependent evolution of the *OPR* in a region with changing temperature is complex, as conversion between the two spin modifications can involve gas phase collisions with H atoms and ions as well as grain surface reactions (Lique et al. 2012; Bron et al. 2016). If conditions in the very small regions being considered here have been evolving, the *OPR* will not simply reflect the temperature, but will depend on the past history of the gas. This likely starts with an extremely low *OPR* at the temperature of the molecular cloud boundary, and increasing when the temperature increases.

The conversion rate of para- to ortho-H₂ conversion by exchange in collisions with H atoms is very slow, $\leq 10^{-15}$ cm³s⁻¹ for $T \leq 400$ K (Lique et al. 2012). This yields a characteristic time scale $\sim 10^5$ yr at a density of 100 cm⁻³, which is significantly longer than the characteristic timescales of TDRs or shocks (discussed below). Thus, the *OPR* is not easily determined by modeling.

Observations of four star-forming regions producing shocked H₂ (Neufeld et al. 2006) suggested two values of the *OPR*: 0.2–0.5 and 1.5–2 for the warm and hot component, respectively. Numerous studies have found that H₂ in photon dominated regions (PDRs), *OPR* ~ 1 despite gas temperatures of several hundred to one thousand K (see references on p.2 of Bron et al. 2016). Given the available information we adopt *OPR* = 1, so that $N(\text{H}_2) = 2N(\text{ortho-H}_2)$. Since the *OPR* is unlikely to be less than unity (a value characteristic of equilibrium at typical diffuse ISM temperatures) and is restricted to be less than 3 (except in very unusual cases) for which $N(\text{H}_2) = 1.33N(\text{ortho-H}_2)$, the uncertainty introduced by our lack of precise information on the *OPR* is modest.

4.3.2. Total H₂ Density and Kinetic Temperature

Solving the rate equation for lowest levels, we can calculate the quantity $n(3)A_{3,1}$ (Equation 5) as a function of the total H₂ density and kinetic temperature (T_{kin}). The result is shown in the upper panel of Figure 7. The lower panel shows the excitation temperature of the *S*(1) line. From a given value of $n(3)A_{3,1}$ we find the required total H₂ density for a given kinetic temperature, as well as the excitation temperature characterizing the degree of excitation of the H₂.

It is evident that a lower kinetic temperature requires a higher total H₂ density to produce the observed emission, and that minimum kinetic temperature of ≥ 200 K is required to have a density $\leq 10^4$ cm⁻³.

In this model, the thermal pressure of the small structures seen in the JWST images is much better constrained than the temperature and density individually. If we exclude the lowest kinetic temperature, we find that for $400 \text{ K} \leq T_k \leq 1000 \text{ K}$ the pressure, P/k is within 10% of $3.5 \times 10^5 \text{ K cm}^{-3}$. This is far greater than that of the CNM, with $\langle P/k \rangle = 3800 \text{ K cm}^{-3}$ (Jenkins & Tripp 2011); $2000 \text{ K cm}^{-3} \leq P/k \leq 10,500 \text{ K cm}^{-3}$ (Goldsmith et al. 2018). It is also far above the pressure measured in diffuse molecular gas, for which P/k is between 4600 and 6800 K cm⁻³ (Goldsmith 2013). The thermal pressure is comparable to that found in TSAS observed in the radio, with $P \simeq 10^6 \text{ K cm}^{-3}$ (Stanimirović & Zweibel 2018). The size of these very small regions, $1 \leq L \leq 100 \text{ AU}$ is comparable to that of the structures we have found in the H₂ *S*(1) emission. The extreme overpressure of the H₂ condensations suggests that their lifetime is limited, but this would be a natural result of their being turbulent dissipation regions or postshock instabilities (discussed below).

We can simplify the problem by considering only the two lowest levels of ortho-H₂ in the excitation calculation. This is justified by the much higher energy of the $J = 5$ level, $E/k = 2333 \text{ K}$ compared to that of $J = 1$, and the much faster spontaneous decay rate, $A_{5,3} = 9.84 \times 10^{-9} \text{ s}^{-1} \simeq 20$ times greater than $A_{3,1}$. The result is that there is negligible population in $J = 5$, as any infrequent collisional excitation of that level decays rapidly to $J = 3$. With the definition $f(3)$ as the fraction of ortho-H₂ in the $J = 3$ level we can write for the total H₂ density

$$n(\text{H}_2) = \frac{n(3)(1 + \text{OPR}^{-1})}{f(3)}. \quad (10)$$

The collision rate is the product of the collision rate coefficient and the total H₂ density since either ortho- or para-H₂ can excite the *S*(1) transition⁴. The upwards collision rate is $C_{1,3} = R_{1,3}n(\text{H}_2)$ and the downwards collision rate

⁴ In Appendix B we determine that the total extinction through the Taurus Molecular Cloud boundary region is $0.2 \leq A_v \leq 1.0 \text{ mag}$, so that the hydrogen will be largely molecular. We also consider only moderate temperatures in *e.g.* postshock regions, which are too low to destroy a significant fraction of the H₂. Thus, assuming the excitation is by collisions with H₂ is reasonable.

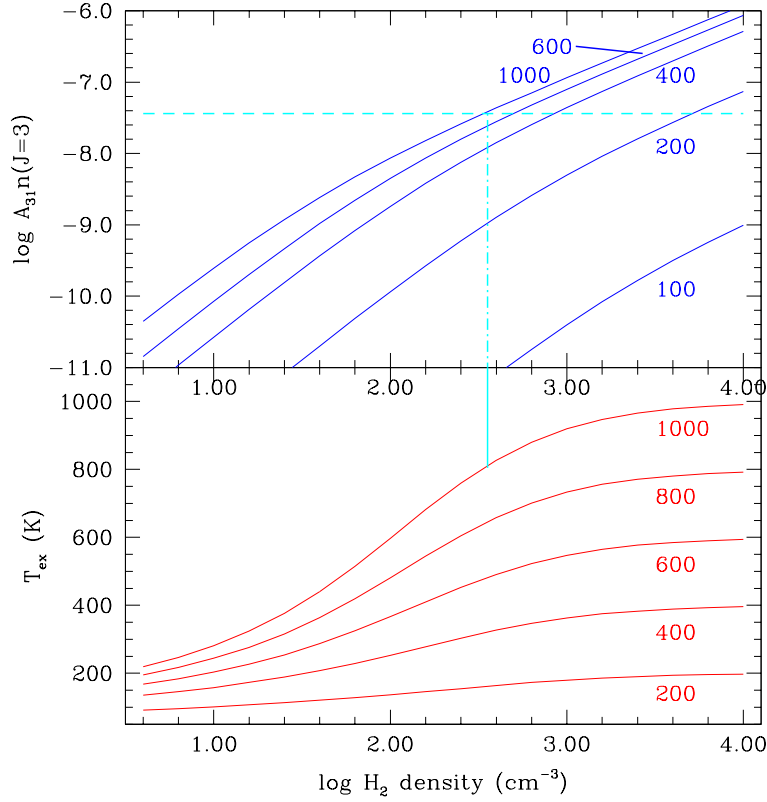


Figure 7. Upper panel: Dependence of the quantity $n(3)A_{3,1}$ characterizing the emission from the $J = 3$ level of ortho- H_2 on total H_2 density and kinetic temperature. The five blue curves are labeled by their kinetic temperature. The horizontal dashed cyan line shows value, $\log(n(3)A_{3,1}) = -7.44$, corresponding to an observed intensity of 10 MJysr^{-1} . The intersection of this line with curve for given kinetic temperature (here 1000 K) determines the total H_2 density (here $\simeq 350 \text{ cm}^{-3}$), as indicated by the vertical dot-dashed cyan line. Lower panel: excitation temperature of the $S(1)$ line as function of total H_2 density and kinetic temperature. The vertical solid cyan line indicates the excitation temperature, 800 K, determined by the selected kinetic temperature and the derived H_2 density.

$C_{3,1} = R_{3,1}n(\text{H}_2)$, with $R_{1,3} = R_{3,1}(7/3)\exp[-(845/T_{\text{kin}})]$. The rate equation gives

$$f(3) = \frac{C_{1,3} + C_{3,1} + A_{3,1}}{C_{1,3}}. \quad (11)$$

Inserting Equation 11 into Equation 10 yields a quadratic equation for $n(\text{H}_2)$, with a solution in the usual form $n(\text{H}_2) = (-b + (b^2 - 4ac)^{0.5})/2a$, where $a = R_{1,3}$, $b = -(1 + OPR^{-1})n(3)(R_{1,3} + R_{3,1})$, and $c = -(1 + OPR^{-1})n(3)A_{3,1}$. For a given $S(1)$ intensity, we have the column density in $J = 3$, $N(3)$, and with the assumed size of the region L , we get the observed density in $J = 3$, $n(3)$. The solution is the total H_2 density as a function of the kinetic temperature.

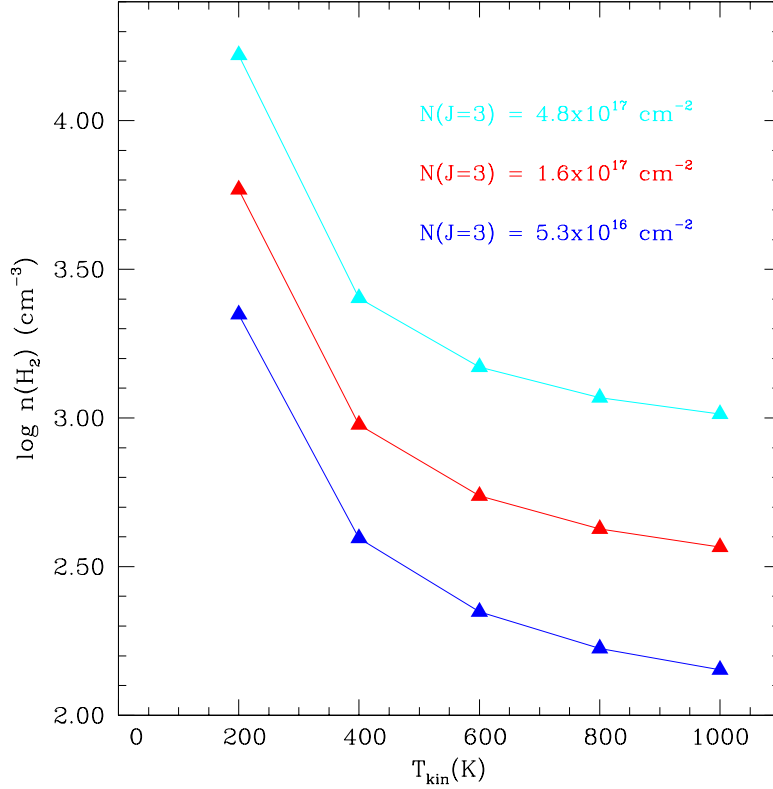


Figure 8. Total H₂ density as function of kinetic temperature for given $J = 3$ column density, $N(J = 3)$. The three curves are for the column density corresponding to intensity 10 MJysr^{-1} , and factor of 3 greater and smaller column density than this.

Figure 8 shows results for the nominal column density $N(3) = 1.7 \times 10^{17} \text{ cm}^{-2}$, and a factor of 3 higher and lower column density.

While lower kinetic temperatures cannot be *a priori* excluded, a total H₂ density $\leq 500 \text{ cm}^{-3}$ required for $T_{kin} \geq 600 \text{ K}$ appears more reasonable than the much higher densities required for lower kinetic temperatures. The total H₂ column density required for $T_{kin} = 200 \text{ K}$ is approximately an order of magnitude larger than that required for $T_{kin} = 600 \text{ K}$. Kinetic temperatures $\simeq 1000 \text{ K}$ are far higher than those found in the quiescent molecular interstellar medium, and appear to be the only explanation for presence of certain ions, particularly CH^+ , for which the key formation reaction is highly endothermic (e.g. [Falgarone et al. 2010a,b](#)). This is clearly vastly hotter than the $10 \text{ K} \leq T_{kin} \leq 100 \text{ K}$ found in the molecular ISM ([Goldsmith 1987](#)) and also the cold neutral medium ([Heiles & Troland 2003](#)). Several mechanisms have been proposed to explain such elevated temperatures in small regions of the ISM, and we briefly discuss these in the following section.

5. PRODUCING THE HIGH KINETIC TEMPERATURE REQUIRED TO EXPLAIN THE H₂ $S(1)$ EMISSION

We here discuss two possible sources for localized heating of the interstellar medium that could explain the structure in the H_2 emission that we have observed with JWST; these are dissipation of turbulence and shocks.

5.1. Dissipation of Turbulence and Small-Scale Heating

Turbulence is well-recognized as a general characteristic of the interstellar medium. As discussed in the review by Falceta-Gonçalves et al. (2014), it is characterized by fluctuations in time and space of various quantities including velocity and density. The general picture is that energy is injected on a relatively large scale, and cascades down to a much smaller scale of tenths of AU on which there is dissipation due to viscosity, which produces local gas heating (Falgarone & Puget 1995).

This led to specific models for turbulent dissipation involving magnetized vortices (Falgarone et al. 1995; Joulain et al. 1998; Godard et al. 2009, 2014). These models have been tailored for a largely atomic medium, but the physical characteristics are in many respects very similar to what we have derived for the small-scale structures seen in the Edge and Peak regions of the Taurus Molecular Cloud boundary. Figure 2 of (Godard et al. 2009) indicates a peak temperature of $\simeq 700$ K at a radius of 50 AU for their reference model, having $n_{\text{H}} = 30 \text{ cm}^{-3}$ and $A_v = 0.4$ mag. This density is a factor $\simeq 10$ lower than the minimum we can find acceptable to explain the density of H_2 in $J = 3$ state. The picture of dissipation in these models is that there are many such small turbulent dissipation regions (TDRs) along the line of sight, so that each has much weaker emission than we observe. However, the range of density and size studied by Godard et al. (2014) comes close to including parameters that would explain our H_2 results.

Lesaffre et al. (2020) carried out a very high spatial resolution modeling of localized heating resulting from dissipation of turbulence. A random velocity field with *rms* velocity 2.1 km s^{-1} in a region with $n_{\text{H}} = 100 \text{ cm}^{-3}$ and $N_{\text{H}} = 1 \times 10^{18} \text{ cm}^{-2}$ led to turbulent dissipation and to the formation of shocks, which raised the temperature to over 1000 K. However, the excitation temperature of the $S(1)$ line ($\simeq 150$ K) is considerably less than we estimate (Figure 7) because the lower density does not provide the required collision rate. Further high-resolution numerical modeling is necessary to understand whether turbulent dissipation operating on the scale of structures we observe and in a largely molecular medium can provide the observed H_2 emission.

5.2. Shocks

Shocks in the interstellar medium perturb the velocity of the gas, increase its density, generally producing also an increase in temperature. There are many different types of shocks, with and without magnetic fields, which differently affect the gas, and various models treat these in different ways, including both individual and multiple shocks being present. Without being comprehensive we here give some of the results that are relevant for H_2 emission. As illustrated by the spectra of H_2 shown by Neufeld et al. (2006), shocks can broaden line profiles, and if the shock velocity is sufficiently large, the presence of shocks can be almost unambiguously identified. Since we are observing regions without significant sources of mechanical energy (*e.g.* young or evolved stars), we expect any shock velocities to be less than the 120 km s^{-1} resolution of JWST MIRI/MRS at $17 \mu\text{m}$ wavelength.

We present ^{12}CO spectra in the directions of the Peak and Edge regions in Appendix B. The line parameters indicate that the hydrogen along these lines of sight is largely molecular. The line profiles of ^{12}CO in both regions clearly suggest that multiple velocity components are present; these are also suggested in the ^{13}CO spectra with marginal signal to noise ratio. In both positions, the velocities of the various components differ by $\simeq 3 \text{ km s}^{-1}$. It is possible that these represent different gas components that are colliding to produce low-velocity shocks. While much higher-angular resolution data would be valuable, we consider the possibility of low-velocity shocks being responsible for the heating of the gas that is responsible for the H_2 emission.

Pon et al. (2012) considered few km s^{-1} shocks propagating in molecular gas with density of 1000 cm^{-3} . These authors found that the $\text{H}_2 S(1)$ intensity could be 5 to 15 times stronger than that found from the photon dominated region (PDR) associated with the molecular cloud, and thus potentially a discriminant between shocks and PDR emission. Subsequent observations (Pon et al. 2015) of mid- J CO lines, particularly the $J = 9 \rightarrow 8$ transition, were interpreted as confirmation of the presence of such shocks. However, the intensities predicted by three models presented in Table 4 of Pon et al. (2012) are ~ 2 orders of magnitude below the Taurus boundary results, so this particular model cannot be explaining our observations.

Kristensen et al. (2023) considered a very large grid of shock models, with different values of initial density, shock velocity, u , and magnetic field parameter $b = B_{\text{transverse}}/n(\text{H})^{0.5}$. The $S(1)$ emission is maximized for the least magnetic shocks ($b = 0.1$), and even for $u = 5 \text{ km s}^{-1}$ is over an order of magnitude weaker than observed, although

the peak temperature and density are significantly higher than required to be consistent with results. Optimization of parameters would plausibly improve the agreement, but the gap between this model and our observations appears significant.

Lesaffre et al. (2013) considered a wide range of shocks of different characteristics, with velocities between 3 km s⁻¹ and 40 km s⁻¹, propagating in media with density between 10² and 10⁴ cm⁻³. These authors find for weakly magnetized shocks in region in which hydrogen is molecular that the maximum temperature is given by

$$T_{max} = 53 \text{ K}(u/1 \text{ km s}^{-1})^2. \quad (12)$$

Thus, a shock velocity of $\sim 3 \text{ km s}^{-1}$ produces a maximum temperature $\sim 500 \text{ K}$. As shown in Figure 1b of Lesaffre et al. (2013), the heated layer in such a low-velocity shock in region with preshock density $n_{\text{H}} = 100 \text{ cm}^{-3}$ has a thickness $\sim 10^{15} \text{ cm}$, comparable to the size of the small-scale structures we observe in the $S(1)$ emission. The total H₂ column density is $1 \times 10^{18} \text{ cm}^{-2}$, very close to what is implied by our results for kinetic temperature = 500 K, $N(\text{H}_2) = 1.4 \times 10^{18} \text{ cm}^{-2}$. The intensity of $S(1)$ emission for a 3 km s⁻¹ shock in their model is 1.4 MJy sr⁻¹, significantly less than we observe. For $u = 5 \text{ km s}^{-1}$, $I_{\nu} = 7 \text{ MJy sr}^{-1}$, approaching the observed value, with temperature somewhat higher, and heated layer thickness smaller. What is not clear is how the density throughout the extended heated layer compares to that we derive, namely $n(\text{H}_2) \simeq 700 \text{ cm}^{-3}$ for $T_{kin} = 500 \text{ K}$ and $n(\text{H}_2) \simeq 400 \text{ cm}^{-3}$ for $T_{kin} = 800 \text{ K}$. More detailed calculations including post-shock instabilities and formation of small-scale structures are necessary to more firmly connect the picture of low velocity shocks and our H₂ observations.

6. SUMMARY AND CONCLUSIONS

We have reported imaging of the $S(1)$ 17 μm line of H₂ with the MIRI/MRS instrument on the JWST. Two regions on the boundary of the Taurus Molecular Cloud having total visual extinction $A_V = 0.2\text{--}1.0 \text{ mag}$ were observed using 4x4 mosaics of pointings to obtain, after some edge cropping, 69 x 81 0.2'' pixels. We see H₂ line emission at high statistical significance throughout most of the two regions, denoted ‘‘Edge’’ (near the relatively sharp boundary of the ¹³CO $J = 1 \rightarrow 0$ emission) and ‘‘Peak’’ (including the location of the strongest H₂ emission observed with *Spitzer*; Goldsmith et al. 2010). The average flux densities for the Peak region and the Edge region are 32.1 MJy sr⁻¹ and 14.5 MJy sr⁻¹ respectively, corresponding to $J = 3$ H₂ column densities of 5.1 and $2.3 \times 10^{17} \text{ cm}^{-2}$.

In addition to the extended emission, there are clearly isolated regions of stronger emission, having angular sizes 1.0''–2.5'', corresponding to physical sizes of 140–350 AU. This is comparable to the tiny scale atomic structure seen in observations at radio wavelengths, but here evident for the first time in the quiescent molecular interstellar medium. A characteristic flux density for these ‘‘clumps’’ is 10 MJy sr⁻¹, corresponding to a column density of H₂ in the $J=3$ level equal to $1.6 \times 10^{17} \text{ cm}^{-2}$.

We have investigated a number of different mechanisms for explaining this emission, which arises from the $J = 3$ level 845 K above the $J = 1$ level (the ground state of ortho-H₂) and 1016 K above the $J = 0$ level (the ground state of para-H₂). Cosmic ray excitation, UV excitation, and H₂ formation cascade excitation all appear inadequate to explain the result in the relatively benign environment of the Taurus Molecular Cloud boundary.

The most plausible mechanism appears to be collisional excitation, dominated by collisions with other H₂ molecules. Assuming a characteristic length scale for the clumps of 1'' ($2.1 \times 10^{15} \text{ cm}$), we determine a set of solutions with given $n(\text{H}_2)$ and T_{kin} that can reproduce the observed 76 cm⁻³ density of H₂ in the $J=3$ state. Higher temperatures are associated with lower densities, and while we cannot exclude, for example $n(\text{H}_2) = 5 \times 10^3 \text{ cm}^{-3}$ with $T_{kin} = 200 \text{ K}$, considerably higher temperatures and lower densities are much naturally produced by two mechanisms that may be responsible for heating the clumps, namely turbulent dissipation and shocks.

A very reasonable solution is $n(\text{H}_2) = 370 \text{ cm}^{-3}$ and $T_{kin} = 1000 \text{ K}$. This temperature can be produced by models of both turbulent dissipation and shocks. Models of turbulent dissipation regions, having been developed in part to explain the abundance of ions such as CH⁺ which require a temperature close to this value to overcome activation barriers and endothermicity of key reactions, produce temperatures on the order of 1000 K. The peak postshock temperature depends on the shock velocity, but modest shock velocities of 3 to 5 km s⁻¹ are also capable of producing such temperatures.

Shock models differ significantly in their predictions for the intensity of the $S(1)$ line, with that of Lesaffre et al. (2013) coming reasonably close to the 10 MJy sr⁻¹ level required, for a weakly magnetized shock ($b = 0.1$) with preshock density 100 cm⁻³ and shock velocity 3 – 5 km s⁻¹. The initial conditions of the modeled shocks typically are atomic gas, but the shock velocity required here is moderate (and so would not produce significant molecular

dissociation) and is similar to that suggested by the extent of the components seen in the ^{12}CO line profile. We hope that future calculations will succeed in both showing the development of small-scale structure in the molecular interstellar medium and explaining the accompanying intense H_2 $S(1)$ line emission that we have observed. JWST MRS studies of the $S(2)$ and $S(3)$ lines will help better constrain the properties, and so the origin, of this hot gas embedded in a quiescent interstellar medium.

We thank Dr. Shmuel Bialy for insightful discussions about H₂ excitation, Dr. Edith Falgarone for valuable information about TDRs, and Dr. David Neufeld for sharing his code for calculating molecular cooling in the type of region we have observed. This research was conducted in part at the Jet Propulsion Laboratory, which is operated by the California Institute of Technology under contract with the National Aeronautics and Space Administration (NASA). Copyright 2025 California Institute of Technology. This research was supported by the Space Telescope Science Institute through funding for JWST Cycle 2 Program GO-03050. X. W. is supported by the National Natural Science Foundation of China (grant 12373009), the CAS Project for Young Scientists in Basic Research Grant No. YSBR-062, the Fundamental Research Funds for the Central Universities, the Xiaomi Young Talents Program, and the science research grant from the China Manned Space Project. X. W. also acknowledges work carried out, in part, at the Swinburne University of Technology, sponsored by the ACAMAR visiting fellowship. G.A.F gratefully acknowledges the Deutsche Forschungsgemeinschaft (DFG) for funding through SFB 1601 “Habitats of massive stars across cosmic time” (sub-project B1) and from the University of Cologne and its Global Faculty programme. Support for R.S. was provided by NASA through the NASA Hubble Fellowship grant # HST-HF2-51566.001 awarded by the Space Telescope Science Institute, which is operated by the Association of Universities for Research in Astronomy, Inc., for NASA, under contract NAS5-26555.

REFERENCES

- Berné, O., Martin-Drumel, M.-A., Schroetter, I., et al. 2023, *Nature*, 621, 56, doi: [10.1038/s41586-023-06307-x](https://doi.org/10.1038/s41586-023-06307-x)
- Beuther, H., Ahmadi, A., Mottram, J. C., et al. 2019, *A&A*, 621, A122, doi: [10.1051/0004-6361/201834064](https://doi.org/10.1051/0004-6361/201834064)
- Bialy, S., Belli, S., & Padovani, M. 2022, *A&A*, 658, L13, doi: [10.1051/0004-6361/202142619](https://doi.org/10.1051/0004-6361/202142619)
- Bialy, S., Burkhart, B., Seifried, D., et al. 2024, arXiv e-prints, arXiv:2408.06416, doi: [10.48550/arXiv.2408.06416](https://doi.org/10.48550/arXiv.2408.06416)
- Black, J. H., & van Dishoeck, E. F. 1987, *ApJ*, 322, 412, doi: [10.1086/165740](https://doi.org/10.1086/165740)
- Brogan, C. L., Goss, W. M., Lazio, T. J. W., & Faison, M. D. 2007, in *Astronomical Society of the Pacific Conference Series*, Vol. 365, SINS - Small Ionized and Neutral Structures in the Diffuse Interstellar Medium, ed. M. Haverkorn & W. M. Goss, 12
- Bron, E., Le Petit, F., & Le Boulrot, J. 2016, *A&A*, 588, A27, doi: [10.1051/0004-6361/201527879](https://doi.org/10.1051/0004-6361/201527879)
- Caselli, P., Walmsley, C. M., Zucconi, A., et al. 2002, *ApJ*, 565, 344, doi: [10.1086/324302](https://doi.org/10.1086/324302)
- Deshpande, A. A. 2007, in *Astronomical Society of the Pacific Conference Series*, Vol. 365, SINS - Small Ionized and Neutral Structures in the Diffuse Interstellar Medium, ed. M. Haverkorn & W. M. Goss, 105
- Falceta-Gonçalves, D., Kowal, G., Falgarone, E., & Chian, A. C. L. 2014, *Nonlinear Processes in Geophysics*, 21, 587, doi: [10.5194/npg-21-587-2014](https://doi.org/10.5194/npg-21-587-2014)
- Falgarone, E., Hily-Blant, P., Pety, J., & Pineau des Forêts, G. 2007, in *Astronomical Society of the Pacific Conference Series*, Vol. 365, SINS - Small Ionized and Neutral Structures in the Diffuse Interstellar Medium, ed. M. Haverkorn & W. M. Goss, 190
- Falgarone, E., Pineau des Forêts, G., & Roueff, E. 1995, *A&A*, 300, 870
- Falgarone, E., & Puget, J. L. 1995, *A&A*, 293, 840
- Falgarone, E., Verstraete, L., Pineau Des Forêts, G., & Hily-Blant, P. 2005, *A&A*, 433, 997, doi: [10.1051/0004-6361:20041893](https://doi.org/10.1051/0004-6361:20041893)
- Falgarone, E., Godard, B., Cernicharo, J., et al. 2010a, *A&A*, 521, L15, doi: [10.1051/0004-6361/201015109](https://doi.org/10.1051/0004-6361/201015109)
- Falgarone, E., Ossenkopf, V., Gerin, M., et al. 2010b, *A&A*, 518, L118, doi: [10.1051/0004-6361/201014671](https://doi.org/10.1051/0004-6361/201014671)
- Farhang, A., Smoker, J., Cox, N. L. J., et al. 2023, *A&A*, 678, A148, doi: [10.1051/0004-6361/202037581](https://doi.org/10.1051/0004-6361/202037581)
- Flagey, N., Noriega-Crespo, A., Boulanger, F., et al. 2009, *ApJ*, 701, 1450, doi: [10.1088/0004-637X/701/2/1450](https://doi.org/10.1088/0004-637X/701/2/1450)
- Flower, D. R. 1998, *MNRAS*, 297, 334, doi: [10.1046/j.1365-8711.1998.01531.x](https://doi.org/10.1046/j.1365-8711.1998.01531.x)
- Forrey, R. C., Balakrishnan, N., Dalgarno, A., & Lepp, S. 1997, *ApJ*, 489, 1000, doi: [10.1086/304827](https://doi.org/10.1086/304827)
- Frail, D. A., Weisberg, J. M., Cordes, J. M., & Mathers, C. 1994, *ApJ*, 436, 144, doi: [10.1086/174888](https://doi.org/10.1086/174888)
- Furuya, K. 2018, in *IAU Symposium*, Vol. 332, *Astrochemistry VII: Through the Cosmos from Galaxies to Planets*, ed. M. Cunningham, T. Millar, & Y. Aikawa, 163–174, doi: [10.1017/S1743921317006810](https://doi.org/10.1017/S1743921317006810)
- Galli, P. A. B., Loinard, L., Bouy, H., et al. 2019, *A&A*, 630, A137, doi: [10.1051/0004-6361/201935928](https://doi.org/10.1051/0004-6361/201935928)
- Gardner, J. P., Mather, J. C., Abbott, R., et al. 2023, *PASP*, 135, 068001, doi: [10.1088/1538-3873/acd1b5](https://doi.org/10.1088/1538-3873/acd1b5)
- Godard, B., Falgarone, E., & Pineau Des Forêts, G. 2009, *A&A*, 495, 847, doi: [10.1051/0004-6361:200810803](https://doi.org/10.1051/0004-6361:200810803)
- Godard, B., Falgarone, E., & Pineau des Forêts, G. 2014, *A&A*, 570, A27, doi: [10.1051/0004-6361/201423526](https://doi.org/10.1051/0004-6361/201423526)

- Goldsmith, P. F. 1987, in *Interstellar Processes*, ed. D. J. Hollenbach & H. A. Thronson, Jr., Vol. 134, 51, doi: [10.1007/978-94-009-3861-8_3](https://doi.org/10.1007/978-94-009-3861-8_3)
- Goldsmith, P. F. 2013, *ApJ*, 774, 134, doi: [10.1088/0004-637X/774/2/134](https://doi.org/10.1088/0004-637X/774/2/134)
- Goldsmith, P. F., Heyer, M., Narayanan, G., et al. 2008, *ApJ*, 680, 428, doi: [10.1086/587166](https://doi.org/10.1086/587166)
- Goldsmith, P. F., Pineda, J. L., Neufeld, D. A., et al. 2018, *ApJ*, 856, 96, doi: [10.3847/1538-4357/aab34e](https://doi.org/10.3847/1538-4357/aab34e)
- Goldsmith, P. F., Velusamy, T., Li, D., & Langer, W. D. 2010, *ApJ*, 715, 1370, doi: [10.1088/0004-637X/715/2/1370](https://doi.org/10.1088/0004-637X/715/2/1370)
- Gredel, R., & Dalgarno, A. 1995, *ApJ*, 446, 852, doi: [10.1086/175843](https://doi.org/10.1086/175843)
- Gry, C., Boulanger, F., Nehmé, C., et al. 2002, *A&A*, 391, 675, doi: [10.1051/0004-6361:20020691](https://doi.org/10.1051/0004-6361:20020691)
- Güdel, M., Briggs, K. R., Arzner, K., et al. 2007, *A&A*, 468, 353, doi: [10.1051/0004-6361:20065724](https://doi.org/10.1051/0004-6361:20065724)
- Heiles, C., & Stinebring, D. 2007, in *Astronomical Society of the Pacific Conference Series*, Vol. 365, SINS - Small Ionized and Neutral Structures in the Diffuse Interstellar Medium, ed. M. Haverkorn & W. M. Goss, 331
- Heiles, C., & Troland, T. H. 2003, *ApJS*, 145, 329, doi: [10.1086/367785](https://doi.org/10.1086/367785)
- Islam, F., Cecchi-Pestellini, C., Viti, S., & Casu, S. 2010, *ApJ*, 725, 1111, doi: [10.1088/0004-637X/725/1/1111](https://doi.org/10.1088/0004-637X/725/1/1111)
- Jenkins, E. B., & Tripp, T. M. 2011, *ApJ*, 734, 65, doi: [10.1088/0004-637X/734/1/65](https://doi.org/10.1088/0004-637X/734/1/65)
- Jones, O. C., Álvarez-Márquez, J., Sloan, G. C., et al. 2023, *MNRAS*, 523, 2519, doi: [10.1093/mnras/stad1609](https://doi.org/10.1093/mnras/stad1609)
- Joulain, K., Falgarone, E., Pineau des Forets, G., & Flower, D. 1998, *A&A*, 340, 241
- Kristensen, L. E., Godard, B., Guillard, P., Gusdorf, A., & Pineau des Forêts, G. 2023, *A&A*, 675, A86, doi: [10.1051/0004-6361/202346254](https://doi.org/10.1051/0004-6361/202346254)
- Lacombe, F., Gendron, E., Rouan, D., et al. 2004, *A&A*, 417, L5, doi: [10.1051/0004-6361:20040030](https://doi.org/10.1051/0004-6361:20040030)
- Langer, W. D., Goldsmith, P. F., Carlson, E. R., & Wilson, R. W. 1980, *ApJL*, 235, L39, doi: [10.1086/183153](https://doi.org/10.1086/183153)
- Langer, W. D., Graedel, T. E., Frerking, M. A., & Armentrout, P. B. 1984, *ApJ*, 277, 581, doi: [10.1086/161730](https://doi.org/10.1086/161730)
- Law, D. R., E. Morrison, J., Argyriou, I., et al. 2023, *The Astronomical Journal*, 166, 45, doi: [10.3847/1538-3881/acdddc](https://doi.org/10.3847/1538-3881/acdddc)
- Le Boulrot, J., Pineau des Forets, G., Roueff, E., Dalgarno, A., & Gredel, R. 1995, *ApJ*, 449, 178, doi: [10.1086/176043](https://doi.org/10.1086/176043)
- Lesaffre, P., Pineau des Forêts, G., Godard, B., et al. 2013, *A&A*, 550, A106, doi: [10.1051/0004-6361/201219928](https://doi.org/10.1051/0004-6361/201219928)
- Lesaffre, P., Todorov, P., Levrier, F., et al. 2020, *MNRAS*, 495, 816, doi: [10.1093/mnras/staa849](https://doi.org/10.1093/mnras/staa849)
- Lique, F., Honvault, P., & Faure, A. 2012, *JChPh*, 137, 154303, doi: [10.1063/1.4758791](https://doi.org/10.1063/1.4758791)
- Liu, M., Krčo, M., Li, D., et al. 2021, *ApJL*, 911, L13, doi: [10.3847/2041-8213/abef6e](https://doi.org/10.3847/2041-8213/abef6e)
- Lorenzetti, D., Giannini, T., Nisini, B., Vitali, F., & Caratti o Garatti, A. 2003, in *Society of Photo-Optical Instrumentation Engineers (SPIE) Conference Series*, Vol. 4834, Discoveries and Research Prospects from 6- to 10-Meter-Class Telescopes II, ed. P. Guhathakurta, 129–138, doi: [10.1117/12.456512](https://doi.org/10.1117/12.456512)
- Marscher, A. P., Moore, E. M., & Bania, T. M. 1993, *ApJL*, 419, L101, doi: [10.1086/187147](https://doi.org/10.1086/187147)
- McCall, B. J., Huneycutt, A. J., Saykally, R. J., et al. 2003, *Nature*, 422, 500, doi: [10.1038/nature01498](https://doi.org/10.1038/nature01498)
- Moore, E. M., & Marscher, A. P. 1995, *ApJ*, 452, 671, doi: [10.1086/176338](https://doi.org/10.1086/176338)
- Narayanan, G., Snell, R., & Bemis, A. 2012, *MNRAS*, 425, 2641, doi: [10.1111/j.1365-2966.2012.21579.x](https://doi.org/10.1111/j.1365-2966.2012.21579.x)
- Neufeld, D. A., DeWitt, C., Lesaffre, P., et al. 2024, *ApJ*, 976, 3, doi: [10.3847/1538-4357/ad83b7](https://doi.org/10.3847/1538-4357/ad83b7)
- Neufeld, D. A., Melnick, G. J., Sonnentrucker, P., et al. 2006, *ApJ*, 649, 816, doi: [10.1086/506604](https://doi.org/10.1086/506604)
- Oka, T., Geballe, T. R., Goto, M., Usuda, T., & McCall, B. J. 2005, *ApJ*, 632, 882, doi: [10.1086/432679](https://doi.org/10.1086/432679)
- Padovani, M., Bialy, S., Galli, D., et al. 2022, *A&A*, 658, A189, doi: [10.1051/0004-6361/202142560](https://doi.org/10.1051/0004-6361/202142560)
- Pon, A., Caselli, P., Johnstone, D., et al. 2015, *A&A*, 577, A75, doi: [10.1051/0004-6361/201525681](https://doi.org/10.1051/0004-6361/201525681)
- Pon, A., Johnstone, D., & Kaufman, M. J. 2012, *ApJ*, 748, 25, doi: [10.1088/0004-637X/748/1/25](https://doi.org/10.1088/0004-637X/748/1/25)
- Roueff, E., Abgrall, H., Czachorowski, P., et al. 2019, *A&A*, 630, A58, doi: [10.1051/0004-6361/201936249](https://doi.org/10.1051/0004-6361/201936249)
- Santangelo, G., Antonucci, S., Nisini, B., et al. 2014, *A&A*, 569, L8, doi: [10.1051/0004-6361/201424748](https://doi.org/10.1051/0004-6361/201424748)
- Savage, B. D., Bohlin, R. C., Drake, J. F., & Budich, W. 1977, *ApJ*, 216, 291, doi: [10.1086/155471](https://doi.org/10.1086/155471)
- Stanimirovic, S., Weisberg, J. M., Hedden, A., et al. 2004, in *Astronomical Society of the Pacific Conference Series*, Vol. 317, Milky Way Surveys: The Structure and Evolution of our Galaxy, ed. D. Clemens, R. Shah, & T. Brainerd, 358
- Stanimirović, S., Weisberg, J. M., Pei, Z., Tuttle, K., & Green, J. T. 2010, *ApJ*, 720, 415, doi: [10.1088/0004-637X/720/1/415](https://doi.org/10.1088/0004-637X/720/1/415)
- Stanimirović, S., & Zweibel, E. G. 2018, *ARA&A*, 56, 489, doi: [10.1146/annurev-astro-081817-051810](https://doi.org/10.1146/annurev-astro-081817-051810)
- Takahashi, J., & Uehara, H. 2001, *ApJ*, 561, 843, doi: [10.1086/323364](https://doi.org/10.1086/323364)

- Tiné, S., Williams, D. A., Clary, D. C., et al. 2003, *Ap&SS*, 288, 377, doi: [10.1023/B:ASTR.0000006062.57984.9c](https://doi.org/10.1023/B:ASTR.0000006062.57984.9c)
- van der Tak, F. F. S., Belloche, A., Schilke, P., et al. 2006, *A&A*, 454, L99, doi: [10.1051/0004-6361:20065289](https://doi.org/10.1051/0004-6361:20065289)
- van der Tak, F. F. S., Black, J. H., Schöier, F. L., Jansen, D. J., & van Dishoeck, E. F. 2007, *A&A*, 468, 627, doi: [10.1051/0004-6361:20066820](https://doi.org/10.1051/0004-6361:20066820)
- Vannier, L., Lemaire, J. L., Field, D., et al. 2001, *A&A*, 366, 651, doi: [10.1051/0004-6361:20000258](https://doi.org/10.1051/0004-6361:20000258)
- Wakker, B. P. 2006, *ApJS*, 163, 282, doi: [10.1086/500365](https://doi.org/10.1086/500365)
- Williams, J. P., Bergin, E. A., Caselli, P., Myers, P. C., & Plume, R. 1998, *ApJ*, 503, 689, doi: [10.1086/306034](https://doi.org/10.1086/306034)
- Wright, G. S., Rieke, G. H., Glaspe, A., et al. 2023, *PASP*, 135, 048003, doi: [10.1088/1538-3873/acbe66](https://doi.org/10.1088/1538-3873/acbe66)
- Xia, J., Tang, N., Zhi, Q., et al. 2022, *Research in Astronomy and Astrophysics*, 22, 085017, doi: [10.1088/1674-4527/ac784e](https://doi.org/10.1088/1674-4527/ac784e)
- Zucker, C., Goodman, A., Alves, J., et al. 2021, *ApJ*, 919, 35, doi: [10.3847/1538-4357/ac1f96](https://doi.org/10.3847/1538-4357/ac1f96)

APPENDIX

A. JWST DATA PROCESSING DETAILS

We here provide a concise overview of the overall processing steps applied to the raw observational data and an introduction to the resulting dataset. The raw MIRI/MRS data were reduced using version 1.16.1 of the STScI pipeline and the CRDS context `jwst_1303.pmap`. It is important to note that data reduced with pipeline versions earlier than 1.15.1 suffer from highly inaccurate error estimates.

In the data reduction process, several non-standard settings were employed, including enabling cosmic ray shower flagging⁵, applying 2D residual fringe correction⁶, and utilizing two different background subtraction algorithms (master background subtraction and pixel-by-pixel subtraction)⁷. Since our primary scientific goals focus on the S(1) and S(2) emission lines, no contamination from hot/warm pixels was detected at the corresponding wavelengths. Thus, manual masking of hot/warm pixels was not performed. However, during subsequent line identification, minor contamination due to hot/warm pixels at other wavelengths was identified. Addressing these contaminants lies outside the scope of this work.

One of the most critical challenges in data processing was reconciling the 4×4 mosaicing design for S(1) with the background subtraction algorithms. Our target is an extended source that spans the observed field, requiring the spatial distribution of its emission lines to achieve our primary scientific objectives. For this purpose, pixel-by-pixel background subtraction was essential to ensure accurate flat-field correction. However, for spectral line identification, results from single exposures with master background subtraction were more suitable. Therefore, we produced datasets processed using both background subtraction algorithms and results without mosaicing for completeness.

To ensure good overlap between adjacent single exposures, it is generally recommended to have a 10% overlap between adjacent pointings in a 4-point dither pattern (in practice, the overlap after a 4-point dither is about 30% in Channel 1). However, it is important to note that the FOVs of the four channels increase with wavelength. To ensure good overlap across all four channels, we have used the FOV of Channel 1 as the reference. This results in a significant increase in overlap from Channel 2 to Channel 4, with Channel 3 having an overlap of about 58%. Considering the 4×4 mosaic observation design, this leads to an interesting phenomenon—our observation depth is not uniform (see Figure 9, and the distribution of the SNR generally decreases from the center to the outer edges. When analyzing the spatial distribution of the data, we must account for the unevenness of the SNR. Given that our focus is on the spatial structure of the molecular clouds, estimating the PSF scale is essential. However, no point sources were available in our observations for PSF modeling, and we consider the 4-point dither and mosaicing processes to have negligible effects on the PSF size. Therefore, we estimated the full width half maximum (FWHM) of the telescope PSF in the MRS wavelength range using the relationship provided by Law et al. (2023),

$$\theta_{\text{FWHM}}(") = 0.033 \lambda(\mu m) + 0.106. \quad (\text{A1})$$

The PSF size directly constrains the lower limit of the molecular cloud structures that can be resolved in our observations. For S(1), this scale is 0.667". Our 4-point dither pattern allows us to Nyquist sample the FWHM of the PSF.

B. CO SPECTRA

We do not have velocity-resolved molecular data with the angular resolution of JWST or even of the size of our mosaiced observations. We do have ¹²CO and ¹³CO $J = 1 \rightarrow 0$ data obtained with 45" – 50" resolution obtained using the FCRAO telescope (Goldsmith et al. 2008). In order to achieve sufficient signal to noise ratio to search for any features due to low-velocity shocks, we averaged data over a region ~8' in size centered on the Edge and Peak positions; the resulting spectra are shown in Figure 10. The line profiles do not appear to change significantly over the regions averaged to produce these spectra and the intensity exhibits only minor variations within each region.

The carbon monoxide emission seen in Figure 10 likely does not come from the heated regions seen in the H₂ S(1) line.

⁵ JWST pipeline cosmic ray snowball/shower information

⁶ JWST pipeline fringing information

⁷ JWST Pipeline background subtraction information

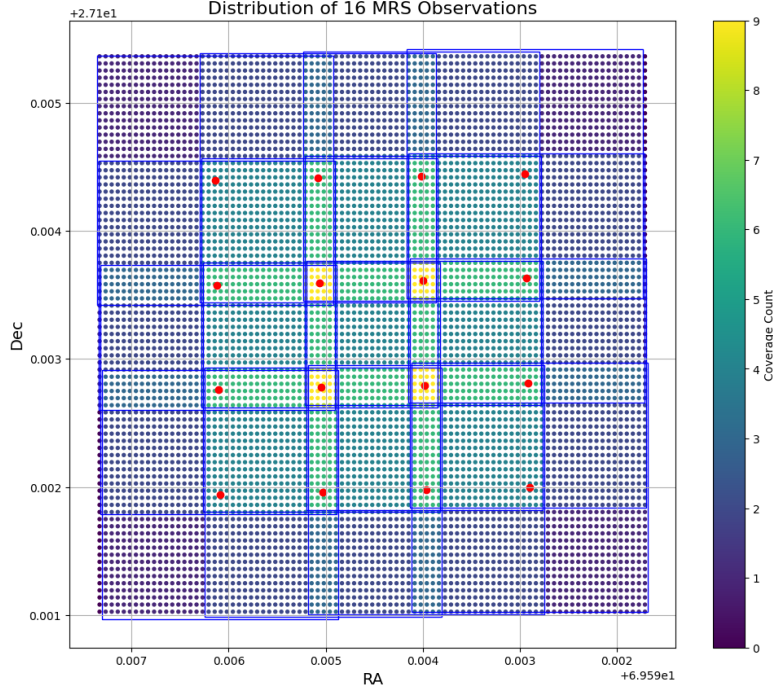


Figure 9. Relative integration times for pixels in the 4 x 4 mosaic of pointings of Sub-band C, Channel 3 MIRI/MRS array used for observations of 17.04 μm $S(1)$ line in the Taurus Boundary regions

Using RADEX (van der Tak et al. 2007), we determine $N(^{13}\text{CO}) = 6.0 \times 10^{14} \text{ cm}^{-2}$ for the Peak and $N(^{13}\text{CO}) = 2.4 \times 10^{15} \text{ cm}^{-2}$ for the Edge, assuming $\delta v = 1 \text{ km s}^{-1}$ FWHM, $n(\text{H}_2) = 100 \text{ cm}^{-3}$, and $T_{\text{kin}} = 20 \text{ K}$. Assuming $N(^{12}\text{CO})/N(^{13}\text{CO}) = 60$, we find peak ^{12}CO line temperatures approximately a factor of 2 greater than observed. To bring the observed and modeled ^{12}CO peak temperatures into agreement would require very low $N(^{12}\text{CO})/N(^{13}\text{CO})$ ratio $\simeq 22$, which could be a result of chemical isotopic fractionation (Langer et al. 1980, 1984; Furuya 2018). It may also reflect variations in temperature and/or density along the line of sight, a filling factor less than unity, or self-absorption, as strongly suggested by the line profile of ^{12}CO in the Edge spectrum. The ^{13}CO column densities suggest H_2 column densities in the range $2\text{--}10 \times 10^{20} \text{ cm}^{-2}$ and thus visual extinctions 0.2–1 mag. This is sufficient for the hydrogen to be largely molecular.

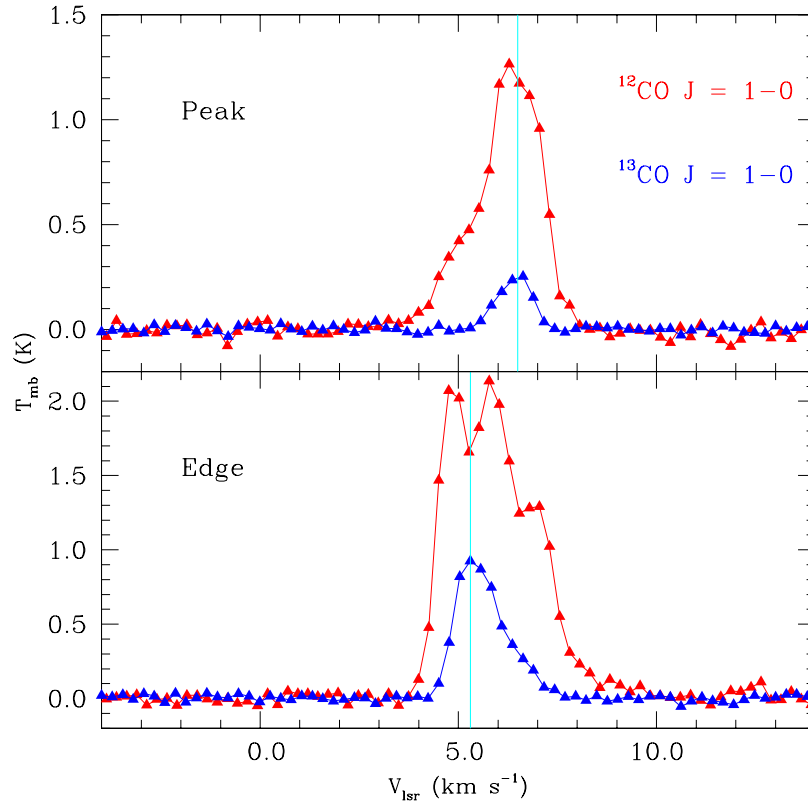


Figure 10. ^{12}CO and $^{13}\text{CO } J = 1 \rightarrow 0$ spectra from survey carried out with 14m FCRAO antenna (Goldsmith et al. 2008). Upper panel: in region encompassing the Peak position. Lower panel: the same lines for region encompassing the Edge position. The vertical cyan lines identify the velocity of the strongest ^{13}CO emission at each position.